PHYSICAL REVIEW B VOLUME 18, NUMBER 9 1 NOVEMBER 1978

A paraelectric system with two electric dipole moments: KI:OH^-

W. M. Kelly*
University of California, Santa Cruz, California, 95064
and University College, Galway, Ireland

Frank Bridges
University of California, Santa Cruz, California 95064
(Received 7 March 1978)

Paraelectric resonance in KI:OH^- at 1.5 and 4.2°K has been measured from 12 to 150 GHz, using a combination of fixed- and swept-frequency techniques. The data confirm the existence of a low-lying excited multiplet of energy levels 140 GHz above the ground-state multiplet and a simple two-multiplet tunneling model is shown to be in good agreement with the main features of the experimental data. The dipole moment of OH^- in the ground-state multiplet is 1.25 e Å, and 2.15 e Å in the excited multiplet, while the dipole orientation in each is $\langle 110 \rangle$. The nearest-neighbor tunneling parameters are dominant, having magnitudes of 8.25 and 13.5 GHz in the lower and upper multiplets, respectively, with a small admixture of second-nearest-neighbor tunneling. The observation of a second multiplet has been interpreted as evidence for a coupled dipole system in which the intrinsic dipole moment of OH^- and the off-center dipole moment can combine in several ways. The swept-frequency experiments, in addition to providing an accurate measurement of some zero-field splittings, show that the absorption line shape is symmetric in frequency at low electric fields. This result implies that internal-electric-field broadening is not a dominant contribution to the linewidths observed in this system.

I. INTRODUCTION

Potassium iodide doped with hydroxyl (KI:OH^-) is a paraelectric system whose behavior has been investigated by a variety of techniques.[1-3] Among these is paraelectric resonance (PER), the use of a microwave spectrometer to detect resonant absorption by dipoles undergoing transitions between the various energy levels. PER is extremely useful in investigating paraelectricity since three important parameters are potentially accessible to direct measurement, namely, the dipole moment, the dipole orientation, and the tunneling parameters.

The initial PER data[3] taken on KI:OH^- between 12 and 75 GHz have some interesting features which provided compelling motivation for the study which is reported in this paper. The observation of lines that move to lower electric fields as the frequency is increased, plus the strong temperature dependence of some resonances[3,4] can apparently be most easily explained by the presence of a second multiplet of energy levels within 200 GHz of the usual ground-state tunneling multiplet. This is an entirely unexpected result which has not been observed in any other paraelectric system. In addition, the KI:OH^- PER spectrum contains an unusually large number of lines, many of which are relatively narrow, which should facilitate a more accurate measurement of the system's parameters. Theoretical work on a two-multiplet tunneling model[5] indicated it would have PER data qualitatively similar to those exhibited by KI:OH^-. Consequently we have carried out a more detailed experimental examination of this system. A preliminary report of some of this work has been published,[6] and in this present paper we present our complete data for KI:OH^- covering 12–150 GHz. The data are shown to be in quite good agreement with a tunneling model[7] extended to include the interaction with a low-lying excited multiplet.[5]

We also include some data taken with a swept-frequency spectrometer near zero electric field. These results suggest that internal electric fields do not contribute significantly to the observed linewidths and therefore other broadening mechanisms must be considered.

The paper is organized as follows: Section II contains a description of the experimental apparatus. The swept-frequency and swept electric field data are then presented in Sec. III followed in Sec. IV by a review of the various theoretical models. In Sec. V the data analysis is outlined and a comparison between data and theoretical models is made. A discussion of these results and the possible origins of additional multiplets of energy levels are given in Sec. VI. Finally, the summary and conclusions are given in Sec. VII.

II. EXPERIMENTAL APPARATUS AND PROCEDURE

A. Fixed-frequency apparatus

For frequencies below 75 GHz a simple reflection spectrometer was used, the details of which have been published previously.[8] Above 75 GHz a transmission spectrometer was used as illustrated in Fig. 1. For these frequencies, harmonic gen-

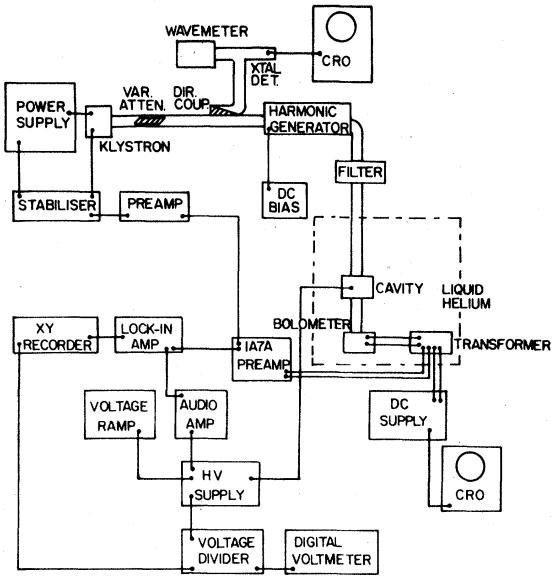

FIG. 1. Spectrometer used above 75 Ghz. CRO: cathode-ray oscilloscope.

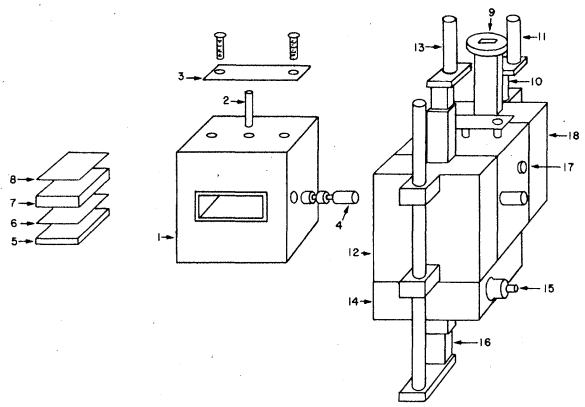

FIG. 2. Transmission cavity assembly: (1) cavity block: (2) quartz tube; (3) brass spring; (4) choke; (5) sample; (6) electrode; (7) quartz spacer; (8) mode suppressor; (9) waveguide flange; (10) input tuner; (11) coupling rod; (12) output waveguide block; (13) output tuner; (14) bolometer mounting block; (15) miniature coaxial sockets; (16) bolometer tuner; (17) earthing screw; (18) input waveguide block.

eration techniques were used to double the klystron's output frequency. The harmonic generator we constructed is similar in design to those used by Gordy *et al.*,[9] and incorporates either point contact or Schottky-barrier diodes. The former were fabricated using tungsten cats whiskers and silicon chips removed from commercial IN23, IN26, or IN53 diodes, while the latter used honeycomb-type wafer diodes from Hughes Corp. detectors. The point-contact diodes produced more harmonic power (−24 dB) when properly tuned but were less mechanically stable than the Schottky-barrier diodes, and more difficult to use. The second harmonic frequency was locked to the resonant frequency of the cavity using a standard klystron stabilizer.

The transmission cavity assembly is illustrated in Fig. 2. The sample sits on the cavity floor with an electrode, quartz spacer, and mode suppressor (to insure only modes with $E_{rf} \| E_{dc}$), on top of it, held firmly[10] in position with a quartz tube and brass spring. The high-voltage lead enters the cavity via a choke which is insulated with several layers of thin (12.5-μm) Mylar tape. The cavity was spark-etched into a brass block; the walls were copper plated and then coated with a thin layer of indium to improve the Q at low temperatures. Power is coupled into the cavity through a circular iris, the amount of coupling being adjustable using a movable short. The transmitted power leaves the cavity through a second iris and is incident on an indium antimonide bolometric detector. Here again a movable short is used to adjust the coupling.

The bolometer is based upon a design of Phillips and Jefferts[11] and is mounted parallel with the microwave electric fields in the center of a short section of waveguide. Its resistance is matched to the waveguide impedance by etching to a suitable thickness, further matching being accomplished by a tuning short. The noise equivalent power is 10^{-13} W. Lock-in detection techniques were used throughout these experiments and resulted in a derivative absorption signal.

B. Swept-frequency apparatus

The swept-frequency spectrometer is illustrated in block form in Fig. 3. Microwave power is transmitted through the sample, which sits in a waveguide immersed in liquid helium, and detected by an indium antimonide bolometer at the end of the waveguide. The dc voltage is used to provide feedback to the sweep generator's leveling circuit (response time 1.0 sec) which ensures a constant power level detected by the bolometer. Lock-in techniques are again used, a voltage modulation being applied to the sample and the small absorption signal detected at the modulation frequency, typically 1–5 kHz.

The waveguide used in the head has a double-ridged cross section; its properties have been detailed by Cohn.[12] It is particularly suitable for this application because for a suitable choice of dimensions, the TE_{20} mode is the only TE_{mn} mode, other than the fundamental, which can propagate between 7.15 and 48.5 GHz, thus hindering the propagation of spurious modes caused by waveguide discontinuities. Figure 4 shows a cross sec-

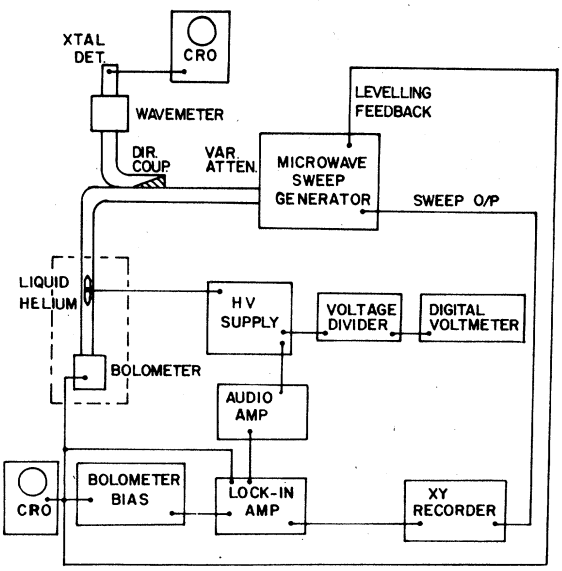

FIG. 3. Swept-frequency spectrometer.

tion through this double-ridged waveguide at the position occupied by the sample. Two potassium-iodide tapers are used to match the impedance of the sample to that of the waveguide. The sample, tapers, and electrode are held in position by a brass spring pushing a sheet of mica through a slot along one waveguide wall. The carbon attenuator is necessary to minimize coherent "noise" in the experimental traces, caused by resonant oscillations within the sample and/or waveguide system.

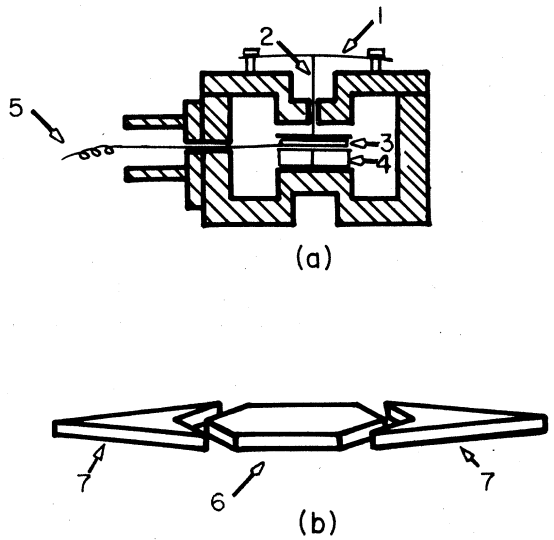

FIG. 4. (a) Cross section through the swept-frequency waveguide: (1) brass spring; (2) mica sheet; (3) carbon attenuator; (4) sample and tapers; (5) high-voltage lead. (b) Side view of the sample (6) and tapers (7).

C. Sample preparation

Samples were prepared from single-crystal boules grown at the Crystal Growth Laboratory of the University of Utah, Salt Lake City, and doped in the melt with the required concentration of KOH. Some boules were grown with one end undoped, so that the pure end could be checked for the absence of unwanted signals. In all cases, the small signals observed in the pure end were several orders of magnitude weaker than the signals from the doped end. After checking that the signal intensity was a linear function of concentration, the rest of the samples were doped with a low OH^- concentration of about 5 ppm.

The crystals were aligned with an x-ray diffractometer before cutting off slices with a string saw and water. These slices were then oriented accurately and lapped flat with a special jig, on a damp linen cloth stretched across a pane of glass. Finished samples, which were generally oriented along ⟨100⟩, ⟨110⟩, or ⟨111⟩ directions were aligned to within $\frac{1}{2}°$.

Great care is necessary to prevent damaging or straining the delicate samples, whose PER absorptions are relatively easy to strain-broaden. Some samples were annealed (in an attempt to narrow the PER signals) by heating them to within 50 °C of their melting point for various lengths of time in an argon atmosphere, and then cooling them very slowly back to room temperature. The signals were not narrowed significantly by this procedure and usually became much weaker.

III. EXPERIMENTAL DATA

A. Swept-frequency data

A zero-field splitting (ZFS), the resonant frequency of a PER absorption with no applied electric field, is difficult to measure accurately with a fixed-frequency spectrometer. Firstly, on a plot of resonant electric field versus frequency, most transitions have strong curvature in the region close to the ZFS, and the resonant frequency is therefore not a linear function of electric field. Consequently the line shape is very nonsymmetric in swept-field experiments when the microwave frequency is close to the ZFS. In addition, it has been shown[13] that if internal electric fields contribute significantly to the PER linewidths then signal distortion is to be expected at low applied electric fields, which shifts the apparent position of the resonance. There is also the difficulty (unless a tunable cavity is used) of finding suitable cavity modes close to the ZFS of the system under study. The use of swept-frequency techniques eliminates the latter problem and also some of the curvature-related distortions; consequently, the accuracy of

ZFS measurements is increased.

Three different resonance transitions were investigated with the swept-frequency spectrometer and the data obtained are incorporated with the fixed-frequency results presented later. Several experimental swept-frequency traces are shown in Fig. 5 for $T=4.2$ K, while the inset shows the three resonance lines on a field-frequency plot. Some of the "noise" on the experimental traces is coherent (i.e., part of the noise is quite repeatable from one trace to the next at a fixed E field. The position of the coherent noise does move, however, with electric field.), caused by reflections in the waveguide system, primarily in the sample, and is the main limitation on the spectrometer's usefulness. The ZFS at 21 and 29 GHz are quite well defined and are more accurately determined in these measurements than in the swept-field experiments.

A very interesting feature of these data (Fig. 5) is the symmetric line shape of the absorption at low fields. To emphasize this symmetry, we have inverted the line about the center crossing and plotted the inverted line (with circles) on top of the original line as shown in the first trace of Fig. 5. From simple considerations we expected a nonsymmetric line in this regime and the observed symmetry is therefore quite surprising. This will be discussed in more detail in Sec. V A.

B. Fixed-frequency data

Most of the data were taken with the frequency of the spectrometer held constant and the electric field swept, usually from 0 to 100 kV/cm. Figure 6 shows a typical trace at $\nu=132.65$ GHz with the positions of the constituent absorptions indicated by the arrows. (The signal shape is derivative due to the detection technique.) The broad dip close to $E=0$ is caused by an absorption whose ZFS is slightly larger than the frequency of the measurement. Traces were taken at various frequencies, and the positions of the resonances plotted as a function of frequency. Figures 7–9 show the conglomerate results of runs, with samples from *four* different crystal boules, for the three main crystal orientations ⟨100⟩, ⟨110⟩, and ⟨111⟩.

Solid lines are included here to indicate data which are believed to be associated with transitions between the same pairs of energy levels, and the resonance "lines" are numbered for ease of reference. Since in some cases, we cannot resolve a line over the entire frequency range this numbering is not unique. For example, lines 16 and 18 of Fig. 8 may be the same line but cannot be resolved between 40 and 85 GHz.

These data have a number of interesting features which we first list below, before discussing them in detail. (i) The number of resonances is large; many are well resolved, but not all. (ii) The intensity of many lines is strongly temperature dependent. (iii) Most lines in Figs. 7–9 have positive slopes ("normal lines") but some lines have negative slopes ("backward lines"—i.e., some lines move to *lower* frequencies as the electric field is *raised*). Such lines turn around at some E field and become normal lines. (iv) Some lines become almost independent of E at some high frequency ν_1 ($\nu_1 > 100$ GHz). Such lines broaden rapidly as ν_1 is approached. (v) The zero-field splittings occur in two distinct groups, one below 50 GHz and the other above 90 GHz. The zero-field splittings of the main lines in these groups are as follows: Lower group: 12.0 ± 1, 21.0 ± 1, 29.0 ± 0.5, 34.0 ± 1.5 (weaker), 40.0 ± 1 GHz. Upper group: 97

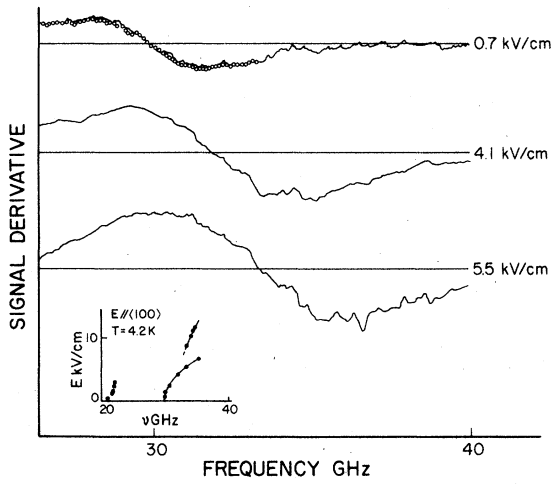

FIG. 5. Experimental swept-frequency traces (derivative line shapes) taken at 4.2 K for $\vec{E} \parallel \langle 100 \rangle$ between 26 and 40 GHz. On the lowest-field trace (0.7 kV/cm) the data were inverted about the zero crossing and is indicated by circles. This shows the high degree of symmetry in the line shape. Inset: The swept-frequency data on a field vs frequency plot.

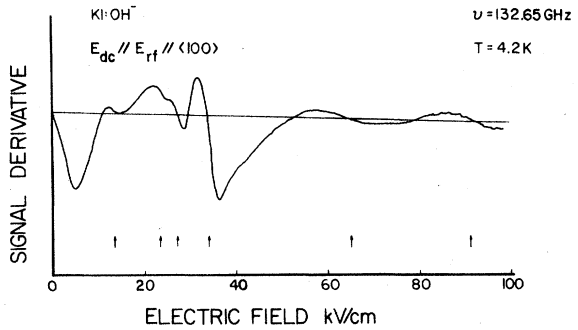

FIG. 6. Typical fixed-frequency experimental trace at 132 GHz for $\vec{E} \parallel \langle 100 \rangle$. The resonances are indicated by arrows.

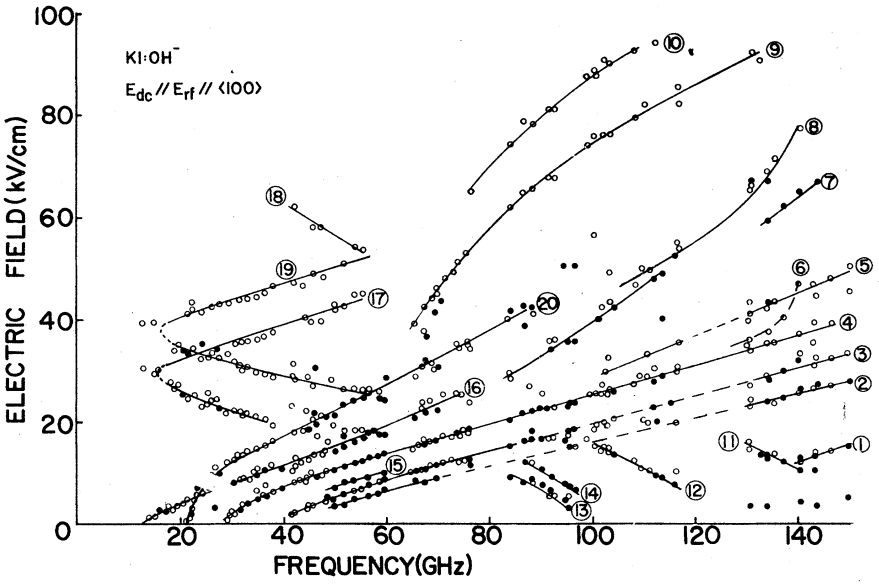

FIG. 7. Experimental data for $\vec{E}_{dc} \| \vec{E}_{rf} \| \langle 100 \rangle$. Solid circles are 1.4-K data. Open circles are 4.2-K data.

± 2.0, 102 ± 3, 115 ± 3, 125 ± 4, 155 ± 5 (weaker). In addition, several splittings exist below 10 GHz (below the range of our spectrometer) while other lines are poorly defined (usually weak) and the zero-field splittings cannot be determined.

The large number of lines of various types with ZFS ranging from below 10 GHz to over 150 GHz is an unusual feature of the KI:OH^- spectrum and should permit a strong test of the theory. However, with so many lines present the problem of resolving the various resonances becomes important and one might well ask if all allowed lines have been observed and whether or not there are important systematic shifts of the apparent resonance position from the actual position. In our decomposition of the lines, we have assumed that the resonances are nearly symmetric (except near a ZFS) and the stronger ones were removed to improve the determination of the weaker lines. To check this procedure we simulated our spectra using the two multiplet ⟨110⟩ model (see Sec. IV B) to determine the field position and intensity of the allowed transitions. Assuming a Gaussian broadening for each line with a linewidth comparable to our better data, a derivative spectrum was obtained such as is shown in Fig. 10. A comparison of the

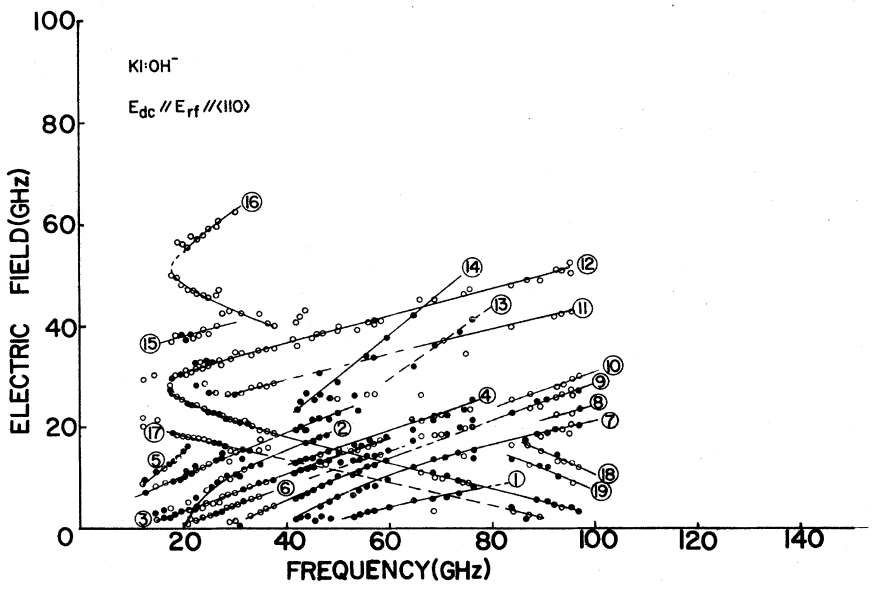

FIG. 8. Experimental data for $\vec{E}_{dc} \| \vec{E}_{rf} \| \langle 110 \rangle$. Solid circles are 1.4-K data. Open circles are 4.2-K data.

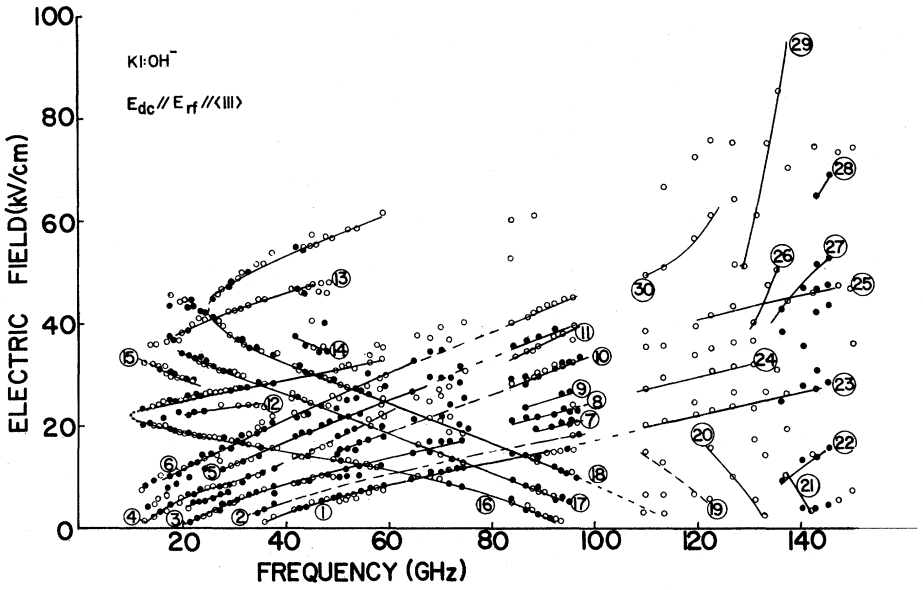

FIG. 9. Experimental data for $\vec{E}_{dc} \| \vec{E}_{rf} \| \langle 111 \rangle$. Solid circles are 1.4-K data. Open circles are 4.2-K data.

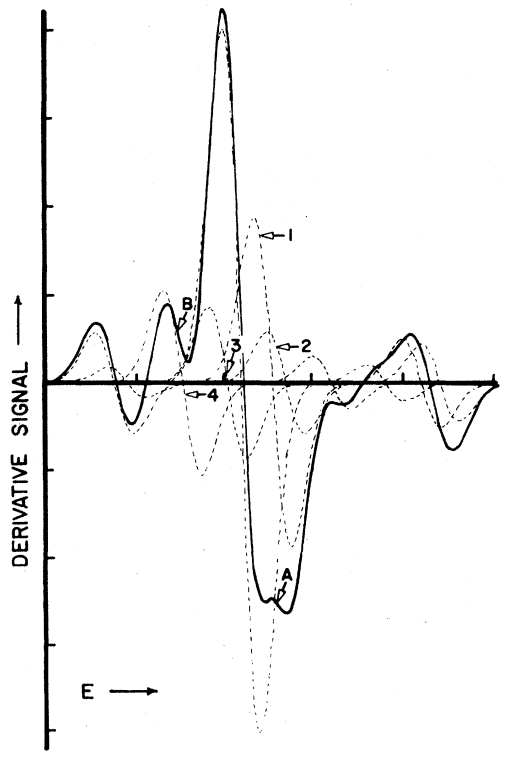

FIG. 10. Predicted experimental line shapes assuming Gaussian resonances. The solid shape is the sum of the component dotted shapes. Lines 1 and 3 near the main resonance are not observed in the total spectrum. Lines 2 and 4 appear as the small lines *A* and *B*.

apparent line positions (solid line) with the actual positions (dotted lines) indicates the following:

(a) The shifts of the main lines are generally small (<3%) but in regions where several lines cross, such as the region near 40 GHz in Figs. 7 and 8, the apparent shifts can be much larger (5–10%).

(b) Some medium strength lines may not be seen when they are close to a strong line (e.g., line 1 in Fig. 10) and two (or more) lines may appear as one line at some intermediate position.

(c) For data with broad lines, not as many lines will be resolved as expected and the shifts may be larger.

(d) The relative intensities of different lines are difficult to estimate from the composite lineshape. For example, line 2 appears as the small line *A* in the total spectrum.

Thus the data should provide a reasonably accurate picture of the main features of the system, but an "exact" fit within the relative errors is clearly not expected. Although the dipole moments obtained from the slopes in Figs. 7–9 should be quite accurate, the experimental line may be shifted from the actual positions or be the weighted average of several lines. These considerations will be included in the later analyses.

Many lines have a strong temperature dependence as indicated in the following examples. Line 15 in Fig. 7 is seen only at 1.5 K (as indicated by solid circles) while line 17 is observed at both 4.2 and 1.5 K but is stronger at 4.2 K. Line 4 is also strongly temperature dependent; at 4.2 K it is one of the strongest lines but at 1.5 K it is very weak.

In addition, several lines are better resolved at 1.5 K, e.g., lines 2, 3, and 15 (Fig. 7) between 50 and 60 GHz. It is not clear whether this is the result of an actual narrowing of these lines or the disappearance of others.

Perhaps the most striking features of the data are the presence of the backward lines over a very wide range in frequency and the occurence of lines at high frequencies which become essentially field independent. Both are unexpected results for the simple tunneling model and support the extension of the model to include a second multiplet.

Finally, some comments on the scatter in the data (Figs. 7–9) are warranted. First, it should be noted that these figures are the composite data of many samples from four different crystal boules. Since some samples had somewhat broader lines (30% broader) the positions were not as well determined and much of the scatter arises from this problem. A related problem occurs at high frequencies where some lines became very steep on the field-frequency plots and consequently have a broad linewidth in swept-field measurements. In some cases (100–120 GHz for $\vec{E}\|\langle 110\rangle$) the presence of such lines makes the analysis virtually impossible.

In addition, some scatter arises from small errors in the magnitude of the electric field, primarily from inaccuracies in the measurement of the sample thickness. These errors should be less than 3% for all samples and less than 2% for most samples.

IV. MODELS

A. Hindered-rotator model

There are two approaches which readily lend themselves to a theoretical description of the properties of paraelectricity.[14] The first is to consider a dipolar impurity as a free rotator whose energy levels are modified in the presence of a *rigid* crystal potential. The Hamiltonian for a free rotator of moment of inertia I is given by

$$\mathcal{H}_R = BJ^2, \tag{4.1}$$

where B, the rotational constant, is inversely proportional to I, and J is the angular-momentum operator. To this is added a cubic crystal potential—usually the first few terms of an expansion in terms of "kubic" harmonics. This model, called the "hindered-rotator model" was first considered in detail by Pauling[15] and later extended by Devonshire[16] and Beyeler.[17] It can be used to describe both diatomic on-center systems and off-center systems when the appropriate moment of inertia is used to obtain B.

Such a model has been used previously to interpret the zero field splittings of one of the first studied OH^- systems—KCl:OH^-. For that case[14] the electric dipole moment orients along the six $\langle 100\rangle$ crystal directions and only the lowest order (nontrivial) kubic harmonic (V_4) is required to provide a potential with $\langle 100\rangle$ oriented minima. Denoting the strength of the potential by K (measured in units of the rotation constant B), the motion is weakly hindered for $K<10$ and strongly hindered for $K>25$.[17] For the strongly hindered case, which corresponds to the situation for most if not all paraelectrics, the lowest six energy levels form a nearly degenerate multiplet that is widely split from the upper levels by an energy many times B. Within this multiplet the energy levels splittings are tiny compared to B.

Most of the known alkali halide:OH^- systems are found to be $\langle 100\rangle$ oriented centers[14] and the simple model with only a V_4 term in the potential expansion provides a reasonable description of the lowest energy levels. However, KI:OH^- is one of the few exceptions for which the minima are not located along $\langle 100\rangle$. Instead, in KI:OH^- they are found to lie along the $\langle 110\rangle$ orientations[6] and the lowest multiplet consists of 12 states. Such a system cannot be explained using only a V_4 potential. Beyeler has shown that a $\langle 110\rangle$ system can be obtained if the next Kubic harmonic, V_6 is included; however, if V_6 is large, it is not obvious that V_8 and higher-order terms can safely be neglected.

To expand this point further we note that from group-theoretical considerations the twelve $\langle 110\rangle$ dipole states will form five distinct energy levels; three triplets with symmetries T_{1u}, T_{2u}, and T_{2g}, a doublet E_g, and a singlet A_{1g}. Although from simple arguments, we expect the totally symmetric A_{1g} state to be lowest in energy, the ordering of the remaining four levels must depend on the form of the interaction. Thus, with only two available parameters in a V_4+V_6 potential, not all orderings of these energy levels can be achieved and higher-order terms are likely necessary. This makes the numerical calculation very lengthy and if electric field effects are also included, such calculations would be extremely time-consuming. The tunneling model discussed in Sec. IV B provides a phenomenological description of a paraelectric system which greatly reduces the necessary computations.

Before going on to the tunneling model, it should be pointed out that within the hindered-rotator model, additional multiplets of energy levels do occur naturally and one might therefore suspect that the hindered-rotator model is the best approach in spite of the additional complications. However, based upon Beyeler's work[17] it appears unlikely that this model can explain the upper energy levels observed in KI:OH^-. This is discussed in Sec. V B.

B. Two-multiplet tunneling model

The other approach is to initially consider the impurity as occupying one of n equivalent potential minima of an infinitely strong crystal potential. If this potential is relaxed, and quantum-mechanical tunneling included, the original n-fold degeneracy is lifted, and the energy levels are split by the tunneling matrix elements. This tunneling model has been developed by several investigators[7,18,19] and is an extension of the early theoretical work on the tunneling inversion of the ammonia molecule. The two-multiplet tunneling model to be described in this section is based upon these simpler tunneling models, consequently, a brief introduction to them is included.

In an alkali-halide crystal the number of potential minima for some given dipole system is not known *a priori*. The three simplest possibilities consistent with cubic symmetry are (i) six equivalent minima in ⟨100⟩ directions, (ii) eight equivalent minima in ⟨111⟩ directions, and (iii) twelve equivalent minima along ⟨110⟩ directions. When no interaction is allowed between dipoles in different potential wells, the system is either 6, 8, or 12-fold degenerate, but allowing a dipole to tunnel between wells partly lifts this degeneracy, and the application of an electric field will further split the levels. For a quantitative treatment of the problem, the directed-basis states illustrated in Fig. 11 are used, where we consider the case with 12 equivalent ⟨110⟩-oriented minima. For example, basis state $|1\rangle$ represents a dipole sitting at the center of the cube and pointing towards the cube edge labeled 1.

The system Hamiltonian $\mathcal{H}$ is written

$$\mathcal{H}=\mathcal{H}_c+\mathcal{H}_{dc}+\mathcal{H}_{rf}\,, \tag{4.2}$$

where $\mathcal{H}_{dc}$ is the contribution from the applied static electric field, $\mathcal{H}_{rf}$ is the contribution from the microwave field, and $\mathcal{H}_c$ is the crystal-field Hamiltonian. In the directed-state representation, $\mathcal{H}_c$ may be written in terms of the "tunneling parameters" η, μ, ν, and σ defined, using the notation of Gomez *et al.*,[7] as follows:

$$\begin{aligned}
&\eta(60^\circ)=\langle 10|\mathcal{H}_c|6\rangle=\langle 5|\mathcal{H}_c|2\rangle\,,\ \text{etc.}\,,\\
&\mu(90^\circ)=\langle 10|\mathcal{H}_c|12\rangle=\langle 5|\mathcal{H}_c|8\rangle\,,\ \text{etc.}\,,\\
&\nu(120^\circ)=\langle 10|\mathcal{H}_c|3\rangle=\langle 5|\mathcal{H}_c|1\rangle\,,\\
&\sigma(180^\circ)=\langle 10|\mathcal{H}_c|9\rangle=\langle 5|\mathcal{H}_c|6\rangle\,.
\end{aligned} \tag{4.3}$$

For example, η represents a 60° rotational tunneling from state $|10\rangle$ to state $|6\rangle$. The resulting symmetric matrix has been tabulated by Gomez *et al.*; we give it in Appendix A for reference.

For the electric dipole Hamiltonian $\mathcal{H}_{dc}$ the matrix is diagonal in the directed-state representation; the entries have also been tabulated in Appendix A for an applied field $E=(E_x,E_y,E_z)$.

Experimentally, E_{dc} was arranged to be parallel with E_{rf} so that the elements of $\mathcal{H}_{rf}(p)$ are similar in form to those of $\mathcal{H}_{dc}(p)$. The complete Hamiltonian is generally impossible to handle analytically and is usually solved numerically to obtain the splittings of the various energy levels as a function of the electric field. For example, Fig. 12 gives a typical computer-generated set of results of the electric-field-frequency dependence, for various transitions, when nearest-neighbor tunneling is dominant and E is parallel to ⟨110⟩.

It is possible to obtain useful information for comparison with the data without solving the problem exactly. Since at high electric fields the energy is primarily due to the interaction with the field, the energy associated with the various minima is clear from inspection, and there will only be a small set of well-defined high-field *slopes* (see Fig. 12) allowed for each model with a particular choice of applied field orientation. Thus, for

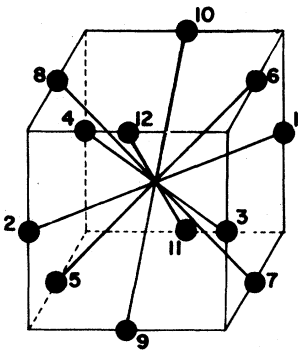

⟨110⟩ DIPOLE ORIENTATIONS

FIG. 11. Directed-state labeling for the ⟨110⟩-dipole model. The dipole in each case is assumed to be at the center of the cube pointing towards the appropriately labeled cube edge.

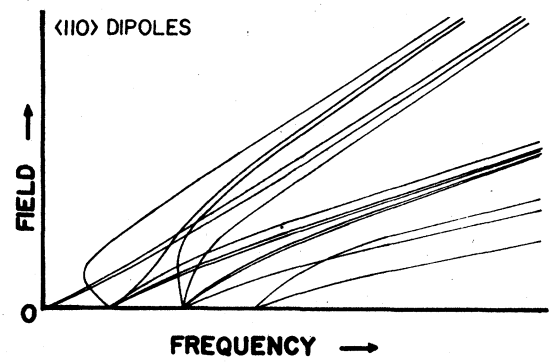

FIG. 12. Exact solution for a ⟨110⟩-dipole model, with an applied electric field in the ⟨110⟩ direction and with tunneling parameters $\eta=1$ and $\mu=\nu=\sigma=0$. The applied field of the allowed transitions is plotted as a function of the resonant frequency.

a ⟨110⟩ system, although many transitions are allowed at most four different slopes are possible and in Fig. 12 only three slopes are observed because of the choice of nearest-neighbor tunneling. The expected slopes for the different tunneling models are summarized in Appendix B for electric fields in the ⟨100⟩, ⟨110⟩, and ⟨111⟩ directions.

Next we consider the extension to the two-multiplet tunneling model. Here, in addition to the usual ground-state multiplet of energy levels, we assume that an excited multiplet exists near enough in energy such that the intermultiplet splitting is comparable to the splittings within a multiplet. These excited states are also assumed to be either ⟨100⟩, ⟨110⟩, or ⟨111⟩ oriented, so in principle there are nine possible multiplet combinations for cubic systems. The simplest of these, the ⟨100⟩-⟨100⟩ model, was investigated earlier.[5] For the present study of KI:OH^-, the ground state is ⟨110⟩ and three combinations must therefore be considered. Although the simplest combinations of multiplets are situations in which the upper and lower multiplets have the same orientations, the potential is not well enough understood to rule out other possibilities *a priori*. For the KI:OH^- system, the two multiplets will be shown to be ⟨110⟩ oriented and this ⟨110⟩-⟨110⟩ model will be treated in detail here. The ⟨110⟩-⟨100⟩ and ⟨110⟩-⟨111⟩ two-multiplet models are introduced sufficiently to enable their rejection as candidates for KI:OH^-.

Figure 13 illustrates the basis states for the three models, where unprimed labels refer to ground states and primed labels to excited states. Each model now has many possible types of tunneling parameters. The ground state of each model considered has the four ⟨110⟩ parameters, $\eta(60°)$, $\mu(90°)$, $\nu(120°)$, and $\sigma(180°)$, together with the excited-state tunneling parameters denoted by primes and the intermultiplet parameters denoted by double primes. For the ⟨110⟩-⟨110⟩ model the new parameters are similar in type to the ground-state parameters: $\eta'(60°)$, $\mu'(90°)$, $\nu'(120°)$, and $\sigma'(180°)$ for the excited states and $\eta''(60°)$, $\mu''(90°)$, $\nu''(120°)$, and $\sigma''(180°)$ between the two multiplets. For the other two models there are differences. The appropriate parameters for the ⟨110⟩-⟨100⟩ model are $\eta'(90°)$, $\mu'(180°)$, and $\eta''(45°)$, $\mu''(90°)$, and $\nu''(135°)$, while the ⟨110⟩-⟨111⟩ model has $\eta'(70.5°)$, $\mu'(109.5°)$, $\nu'(180°)$, and $\eta''(35.3°)$, $\mu''(90°)$, $\nu''(144.7°)$. The qualitative behavior which one expects from a two-multiplet model is illustrated in Fig. 14. Some resonance lines (on the field versus frequency diagram) will be "normal," with a small ZFS and strong intensity at 1.4 K. These correspond to type-*A* transitions on Fig. 14. Transitions like *B* have similar ZFS but will have a weaker relative intensity at 1.4 K than at 4.2 K. Transitions of type *C* give rise to backward-type

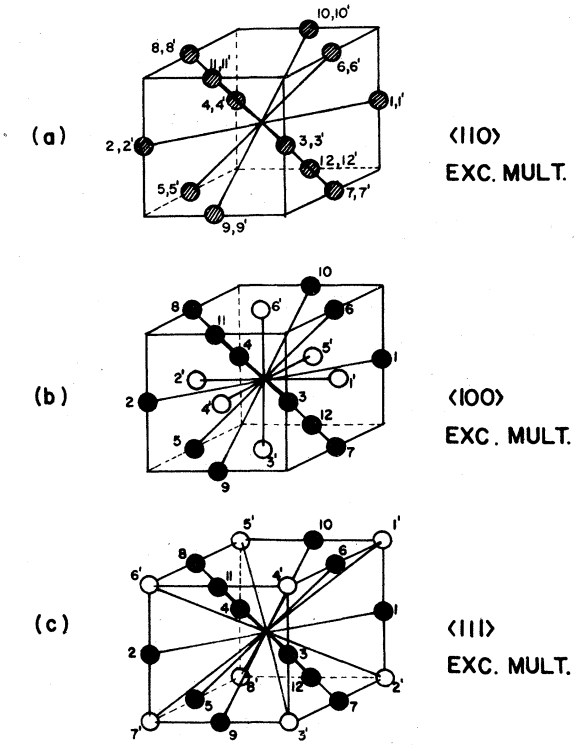

FIG. 13. Directed-basis states for the two-multiplet tunneling models with the ground state consisting of ⟨110⟩-oriented dipoles.

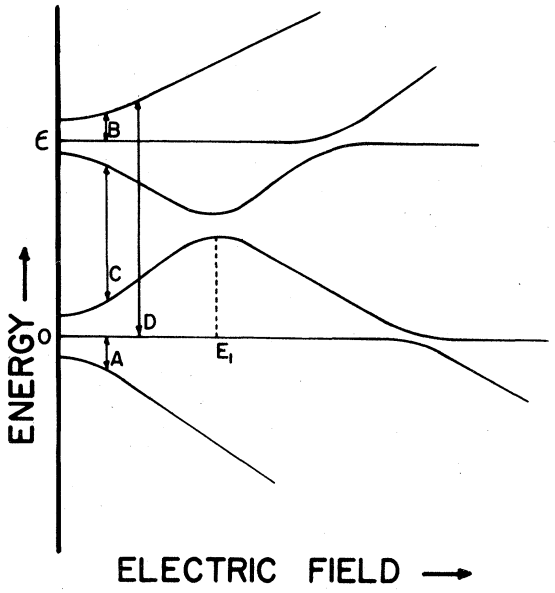

FIG. 14. Some types of resonances expected within a two-multiplet tunneling model. *A*, normal ground-state resonance; *B*, normal excited-state resonance; *C*, backward resonance; *D*, normal line with high zero-field splitting.

lines which start with a negative slope on a field versus frequency diagram, and then turn around and have a positive slope above E_1, giving characteristics similar to the "backward" lines of the data. There will also be a group of normal looking resonances which have large ZFS, such as D. It is possible at this stage, by inspection of Fig. 14 and similar figures for other field orientations, to tabulate the high-field behavior expected of the resonant transitions for each model. This is done in Appendix C for the $\langle 110\rangle$-$\langle 110\rangle$ model.

For an exact numerical solution of the $\langle 110\rangle$-$\langle 110\rangle$ model one proceeds as follows. Assume a ground-state multiplet centered about zero energy, an excited multiplet centered about an energy ϵ, with dipole moments p and p' in the lower and upper multiplets, respectively. Then the Hamiltonian $\mathcal{H}$ is given by

$$\mathcal{H}=\mathcal{H}_c^* +\mathcal{H}_{dc}^* +\mathcal{H}_{rf}^* , \tag{4.4}$$

$$\mathcal{H}_c^* =\begin{pmatrix}\mathcal{H}_{11} & \mathcal{H}_{12}\\ \mathcal{H}_{21} & \mathcal{H}_{22}\end{pmatrix}. \tag{4.5}$$

$\mathcal{H}_{11}$ and $\mathcal{H}_{22}$ describe the behavior of states within the lower and upper multiplets, respectively, while $\mathcal{H}_{12}$ and $\mathcal{H}_{21}$ contain the intermultiplet matrix elements. Then clearly

$$\mathcal{H}_{11}=\mathcal{H}_c(\eta,\mu,\nu,\sigma), \tag{4.6}$$

$$\mathcal{H}_{22}=\mathcal{H}_c(\eta',\mu',\nu',\sigma')+\epsilon I, \tag{4.7}$$

and

$$\mathcal{H}_{12}=\mathcal{H}_{21}=\mathcal{H}_c(\eta'',\mu'',\nu'',\sigma''), \tag{4.8}$$

where $\mathcal{H}_c$ is given in Appendix A, and I is the identity matrix. Terms of the form $\langle i'|\mathcal{H}_c|i\rangle$, i.e., connecting the ground and excited multiplets in the same well, are not included since in general they are expected to be of smaller magnitude. When included in a $\langle 100\rangle$-$\langle 100\rangle$ model and set equal to the largest of the other parameters, very little difference occurred in the predicted spectrum.

The dipole Hamiltonian (for the dc applied field) $\mathcal{H}_{dc}^*$ is again diagonal,

$$\mathcal{H}_{dc}^*=\begin{pmatrix}\mathcal{H}_{dc}(p) & 0\\ 0 & \mathcal{H}_{dc}(p')\end{pmatrix}, \tag{4.9}$$

where the diagonal elements of $\mathcal{H}_{dc}$ are also tabulated in Appendix A. $\mathcal{H}_{rf}^*$ is of a similar form, with E_{dc} replaced by E_{rf}.

The complete Hamiltonian was diagonalized on a PDP11 computer and the allowed transitions calculated for various values of applied field, together with the Boltzmann-corrected transition intensities.

V. ANALYSIS

A. Swept-frequency line shape

The most surprising result from the swept-frequency experiments is the symmetric shape of the absorption line near $E=0$. This was unexpected,

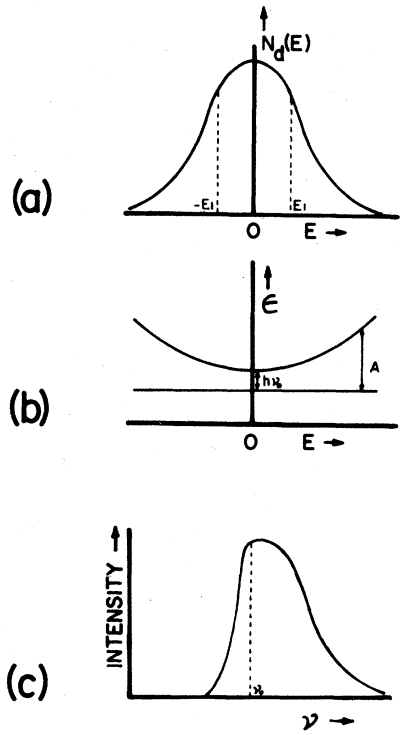

FIG. 15. Theoretical swept-frequency line shapes assuming inhomogeneous electric-field broadening. (a) The number of dipoles N_D (E) in an internal field E, as a function of E. (b) A pair of energy levels as a function of electric field, with an allowed transition (A) between them. (c) The line shape expected of transition A with no applied electric field.

and as the following remarks show, is an important result.

Since paraelectric defects interact strongly with both electric and stress fields, and since real lattices are known to contain random internal strains and electric fields, one might expect either or both of these to contribute significantly to the PER linewidth at $E=0$.

However, if internal electric fields are the primary-broadening mechanism, then it is easy to show that a nonsymmetric line shape would result close to the ZFS. For this discussion we consider a line whose frequency increases monotonically with electric field, consistent with the behavior of the line in Fig. 5. Such a transition will behave similarly to a simple two-level system. We represent the internal electric field distribution by a Gaussian function and hence the dipole distribution as a function of field will be qualitatively as in Fig. 15(a). When there is no applied stress, the energy levels of a PER system are symmetric under inversion of E as in Fig. 15(b), therefore the shape of the absorption as a function of frequency will be as in Fig. 15(c), when no external field is present. Then $N_d(0)$ dipoles sit at $E=0$ and resonate at ν_0,

while $N_d(+E_1)$ and $N_d(-E_1)$ dipoles have local fields of $\pm E_1$, and resonate at the same frequency $\nu_1 > \nu_0$, etc. Near ν_0 the line shape depends upon other broadening mechanisms, and must be quite steep as in Fig. 15(c) if internal electric fields are assumed to be the dominant mechanism. Thus, broadening via electric-field results in a very nonsymmetric line-shape profile. The symmetry displayed by the experimental traces is therefore seen to rule out electric-field broadening for electric fields near $E = 0$ and other mechanisms must be considered.

Several other interactions have been previously investigated as possible broadening mechanisms; a dipole-dipole coupling (via either the stress or electric dipole) and broadening via internal stress in the crystal. At the low concentrations used here, the dipole-dipole coupling should be negligible and we consider briefly the line shape which would result from random internal stress. Here the question of line-shape symmetry is not so easily answered because the energy levels need not be a symmetric function of the stress P, and the energy splitting for an allowed PER transition can be larger or smaller than the ZFS depending on whether the stress is a tension or a compression. Dischler[20] has considered the stress broadening of PER lines, particularly for the KCl:Li^+ system, but investigated primarily the case of fixed-frequency, swept-electric-field measurements. He does, however, give the transition matrix element as a function of frequency at $E = 0$. For this case the line at the ZFS is nonsymmetrically broadened and may be shifted in frequency. This suggests that nonsymmetric swept-frequency line shapes near $E = 0$ should also be expected with stress broadening.

In our measurements, the situation is further complicated through the use of an electric field modulation for our signal detection scheme. Thus, for a fixed, small electric field modulation, the shift of the energy-level splitting is not the same at all values of the stress, and consequently additional asymmetries in the line shape should occur. We have investigated briefly the swept-frequency derivative line shape for a simple four fold dipole system (oriented along the $\pm x$ and $\pm y$ axes) with E-field modulation. These calculations indicated that if internal stress (assuming a symmetric distribution peaked at zero) is the main broadening mechanism, then strongly nonsymmetric derivative line shapes should occur, with an A/B ratio >2 (A is the height of the positive lobe and B the height of the negative lobe of the derivative signal) when the Q of the line ($Q = \nu/\Delta\nu$) is less than 10. Although this does not prove that strain broadening always gives nonsymmetric swept-frequency lines at zero field, it clearly supports such an assertion. Therefore other possible broadening mechanisms, which might account for the observed symmetric line shape, need to be considered.

One type of broadening which also leads to a symmetric line shape is lifetime broadening, arising from the interaction with thermal phonons. Defining a relaxation time by the expression

$$2\pi\Delta\nu\tau \simeq 1 , \tag{5.1}$$

gives a value $\tau \simeq 5\times10^{-11}$ sec for a linewidth of 3.2 GHz. This is considerably faster than the estimate of the dipole-lattice relaxation time $\tau \sim 10^{-9}$ sec obtained by Kapplan and Lüty[2] at 1.35 K. Thus it seems unlikely that this can explain our results.

A second possibility is that the tunneling parameter varies slightly throughout the crystal. Such a variation might arise through the "dressing" of the tunneling element[21,22]

$$\Delta = \Delta_0 e^{-W} . \tag{5.2}$$

Here Δ_0 is the bare-tunneling element and W depends on the stress-coupling constants of the dipole system and the mass of the neighboring atoms. Since W is an exponent, and in many cases $W \gg 1$, then only a small change in W is needed to produce an appreciable change in Δ, and a symmetrical variation of W would lead to a nearly symmetric swept-frequency derivative line shape. This will be discussed in a separate paper.

In view of these limited results, further study of the swept-frequency line shape for this and other systems appears promising. In particular it would be interesting to check whether or not the line shape of KCl:Li^+ is symmetric near zero field since other investigators have interpreted the linewidth in terms of internal stains and/or electric fields.[20,23-25]

B. Difficulties with the hindered-rotator model

Before presenting our analysis in terms of the two-multiplet model it is appropriate to first indicate why we believe the simple hindered-rotator model, as extended by Beyeler,[17] does not explain our data. Consider Fig. 16 which illustrates, for $E = 0$, the energy levels of a hindered rotator as a function of crystal potential K. For an on-center OH^- ion with a rotational constant $B = 18\ cm^{-1} = 540$ GHz, the model clearly does not give the position of the observed second multiplet. For the value of K at which the lowest multiplet is only 50 GHz wide, the next-lowest multiplet occurs at a very high energy.

The larger dipole moment observed in KI:OH^- compared with other OH^- systems indicates that OH^- is off center and this effect should also be included in the effective moment of inertia. We can proceed in two ways. First we can assume that the lattice remains essentially unchanged and esti-

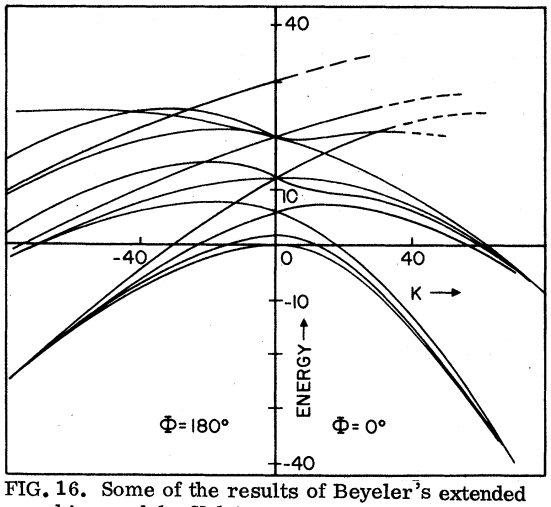

FIG. 16. Some of the results of Beyeler's extended Devonshire model. K determines the strength of the crystal potential and Φ is the parameter determining the dipole orientation (it actually controls the relative admixture of spherical harmonics of order 4 and 6 in the crystal potential). Energy is in units of the rotation constant B.

mate from the known ionic radii, the largest off-center position possible along a ⟨110⟩ orientation. (This is likely an overestimate.) Assuming the OH^- ion is comparable in size to F^- we obtain a maximum off-center position of approximately 0.75 Å. This is turn leads to a much lower value of B of order 50 GHz. Even when the energy levels in Fig. 16 are rescaled for such a value of B, the lowest excited multiplet is still over 300 GHz above the ground-state multiplet. (The experimental splitting is approximately 140 GHz.)

A second approach is to try to estimate a value of B that would correspond to an intermultiplet splitting ϵ_1, that is three times larger than the splitting within the lowest multiplet ϵ_2. However, for the combination of potentials considered by Beyeler, none show two well-defined, 12-fold multiplets for small K. This might well arise from the particular choices of the V_4 and V_6 contributions to the potential used in that work and does not rule out the possibility of two such multiplets. We obtained an estimate of B for the case of a ⟨110⟩ lower multiplet by considering the value of K at which the next-highest energy level is $2\epsilon_2$ above the lowest multiplet. This gives $B \simeq 15$ GHz and corresponds to an off-center position that is more than 50% larger than our estimate from the ionic radii. Such a large off-center position would lead to a very strongly hindered or frozen dipole position. Experimentally, however, the zero-field tunneling splittings are large and the reorientation times are short. These conflicting results indicate the problems that arise if one attempts to use the model of a hindered rotator in a *rigid* cubic lattice to analyze our results and we have therefore excluded it from further consideration.

It should be pointed out that this model omits the motion of the nearest-neighbor atoms as the dipole rotates. Including such motions would increase the moment of inertia and hence might give a small value of B without a large off-center position. Further extensions of the model are necessary to check this possibility.

C. Two-multiplet model

Several features of the data—the backward lines, two groups of zero-field splittings, and a strong temperature dependence of the intensity for some lines—clearly indicate the presence of additional energy levels above the ground-state multiplet. However, without a solid theory for the origin of these additional states, one does not know *a priori* if these states form one or more additional multiplets. In this section we analyze the data under the assumption that only one additional multiplet exists to obtain a phenomenological understanding of the KI:OH^- system. The possibility of several multiplets will be discussed in more detail in Sec. VI.

We start with the determination of the dipole orientations and dipole moments in each multiplet. Using the temperature dependence of the *major* lines and the size of their zero-field splittings we isolated the transitions that occur within the ground-state multiplet and obtained the slopes of each line in the high-field linear region. Then the dipole orientation was obtained by comparing the experimental slopes with those predicted by the three dipole models (Appendix B). A glance at Appendix B shows that a ⟨111⟩-dipole model would only allow one type of slope for $\vec{E} \| \langle 100 \rangle$, while a ⟨100⟩-dipole model would allow only one type of slope for $\vec{E} \| \langle 111 \rangle$. Both of these requirements are incompatible with the data of Fig. 7–9 leaving only the ⟨110⟩ model consistent with our results for the lower multiplet. Once the orientation is known, it is trivial to deduce the dipole moment from the measured slopes. However, to obtain an accurate value for p, one must take into consideration that the data is not really in the high-field limit. This leads to corrections of order 7%. The result for the ⟨110⟩ ground-state multiplet was obtained earlier:

$$p = 1.25 \pm 0.07\, e\,\text{Å}. \qquad (5.3)$$

One might suspect that the lower-multiplet tunneling parameters could also be obtained by this "multiplet isolation" but, because of the strong influence of the excited multiplet on the splittings in the lower multiplet, such a procedure could lead to large errors in the determination of these parameters.

For the upper multiplet, the isolation of the lines is more difficult because these transitions are

much weaker, as a result of thermal depopulation of the upper states, and their intensities are difficult to estimate accurately. Fortunately line 4 in the $\vec{E}\|\langle 100\rangle$ data in Fig. 7 is a well-defined line with a very strong temperature dependence and hence belongs to the upper multiplet. Further its slope is not compatible with the dipole moment obtained for the lower multiplet. Using this well-defined line and Appendix B, one can draw up a complete list of the possible approximate values of the upper multiple dipole moment p' for the various dipole models. These are

$$\begin{aligned} &\langle 100\rangle \text{ model, } p' = 0.72\ e\,\text{Å or } 1.44\ e\,\text{Å};\\ &\langle 111\rangle \text{ model, } p' = 1.25\ e\,\text{Å only;}\\ &\langle 110\rangle \text{ model, } p' = 1.02\ e\,\text{Å or } 2.04\ e\,\text{Å}. \end{aligned} \tag{5.4}$$

To differentiate between these possible models and dipole moments, we then considered the backward lines which are transitions between the two multiplets. The slopes of these lines are determined by p and p' as given in Appendix C for the $\langle 110\rangle$-$\langle 110\rangle$ model. In particular we note that the smallest slope, produced by the largest combination of p and p', provides a means of separating the above possibilities. If the smallest experimental slope is *smaller* than the predictions for a particular model, then that model can be excluded. (Note that the relatively large zero-field splittings will tend to make the experimental slopes somewhat *larger* than that obtained by considering p and p' alone.) A comparison of the lowest experimental slope with the predictions for the 5 possibilities above is given in Table I for each direction of electric field. The lowest slope backward line for $\vec{E}\|\langle 100\rangle$ data excludes a $\langle 111\rangle$ model, a $\langle 100\rangle$ model with $p' \simeq 0.7\ e$ Å and a $\langle 110\rangle$ model with $p' \simeq 1\ e$ Å. Similarly the lowest slope backward line for $\vec{E}\|\langle 111\rangle$ excludes both of the $\langle 100\rangle$ models (with $p' = 0.72$ and $1.44\ e$ Å) and a $\langle 110\rangle$ model with $p' \sim 1\ e$ Å. This leaves only a *$\langle 110\rangle$ model with* $p' \sim 2.0\ e$ Å as a possible choice consistent with the backward lines.

A consistency check on the orientation and dipole moment of the upper multiplet is obtained from the electric field E_T at which the backward lines turn around; e.g., line 16 in Fig. 9 turns around at $E_T \simeq 21$ kV/cm. E_T is determined primarily by the dipole moments p and p' and the intermultiplet splitting ϵ, with minor shifts arising in some cases from the tunneling parameters.

For example, by examining the high-field slopes for the various absorption lines in a $\langle 110\rangle$-$\langle 110\rangle$ model (Appendix C) and ignoring small shifts due to tunneling parameters, we find that the *lowest* E_T will occur when transition B (Appendix C, $\vec{E}\|\langle 111\rangle$) goes through its minimum splitting. This occurs at the "crossing" of the energy levels ϵ_a and ϵ_b given by

$$\epsilon_a = 2pE/\sqrt{6}\ , \tag{5.5}$$

$$\epsilon_b = \epsilon - 2p'E/\sqrt{6}\ . \tag{5.6}$$

For these levels E_T is given by

$$E_T = \sqrt{6}\,\epsilon/2(p+p')\,. \tag{5.7}$$

Similar results are obtained for other turning fields. Thus knowing the possible values of p and p' for a given model one can calculate ϵ from one of the experimental values of E_T and then predict, on the basis of the model, the other values of E_T that might be observed. This procedure was carried out for each of the models and possible dipole moments considered above and the best consistency is obtained using a $\langle 110\rangle$-$\langle 110\rangle$ model with $p' \sim 2$ Å and $\epsilon \simeq 140$ GHz.

The final parameters to be determined are the tunneling parameters. Here there is no clear-cut way of separately determining each of the 12 parameters. We first used all of the known zero-field splittings to find those groups of tunneling parameters that would fit. This was accomplished using a computer search program to check *all* combinations of normalized tunneling parameters in steps of 0.1 from 0 to 1.0. Once these groups of parameters were known, numerous computer spectra were generated for the $\langle 110\rangle$-$\langle 110\rangle$ model starting with $p' \simeq 2.04\ e$ Å and $\epsilon \cong 140$ GHz. About 50 different combinations of parameters were considered for at least one orientation of electric field, with the most promising results of these calculations then checked for the other field orientations. The values of p' and ϵ were also varied slightly around their starting values. The best overall fit was obtained with the following parameters,

$$\begin{aligned} &p = 1.25 \pm 0.06\ e\,\text{Å},\quad p' = 2.15 \pm 0.10\ e\,\text{Å},\\ &\epsilon = 140\ \text{GHz} \pm 10\ \text{GHz},\\ &\eta, \mu = 8.25\ \text{GHz} \pm 10\%,\quad 1.0\ \text{GHz} \pm 50\%,\\ &\eta', \mu' = 13.5\ \text{GHz} \pm 10\%,\quad 2.4\ \text{GHz} \pm 50\%,\\ &\eta'' \simeq 5\ \text{GHz},\\ &\nu, \sigma, \nu', \sigma', \mu'', \nu'', \sigma'' \simeq 0. \end{aligned} \tag{5.8}$$

TABLE I. Comparison of smallest experimental backward slope with the model predictions.

Field orientation	Smallest experimental backward slope	$\langle 110\rangle$-$\langle 110\rangle$ model $p' = 1.02$	$p' = 2.04$	$\langle 110\rangle$-$\langle 100\rangle$ model $p' = 0.72$	$p' = 1.45$	$\langle 110\rangle$-$\langle 111\rangle$ model $p' = 1.25$
$\langle 100\rangle$	0.213	0.257	0.177	0.257	0.177	0.257
$\langle 111\rangle$	0.190–0.200	0.223	0.153	0.288	0.222	0.182
$\langle 110\rangle$	0.230–0.260	0.182	0.125	0.235	0.182	0.182

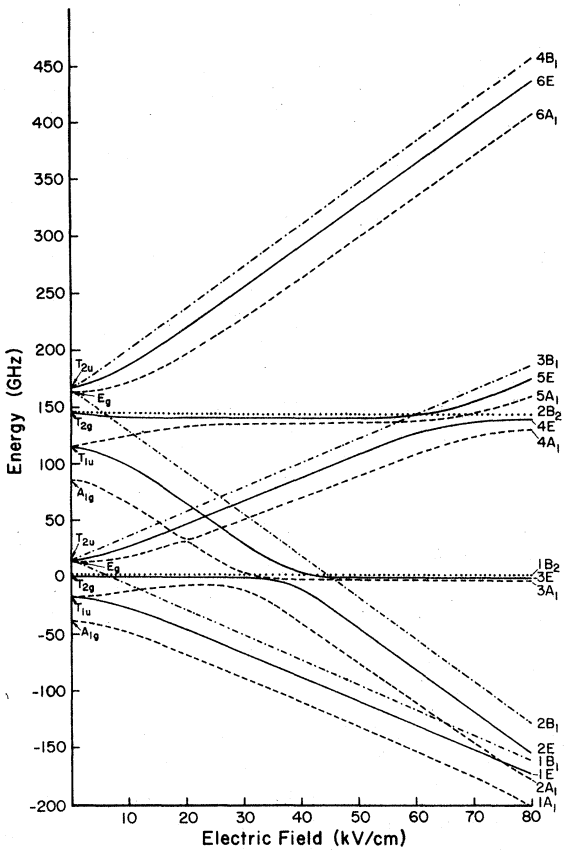

FIG. 17. Energy levels for the two-multiplet model with $\vec{E} \parallel \langle 100 \rangle$ and the tunneling parameters given in Eq. (5.8). The E states are denoted by solid lines, the A_1 states by dashed lines, the B_1 levels by dot-dash lines, and the B_2 levels by dotted lines. Note the repulsion of states of the same symmetry when they approach each other.

The resulting energy-level diagrams for various orientations of electric field have many energy levels with numerous crossings over the range of fields 0–80 kV/cm. To provide some insight into the details of the energy-level structure we have given the complete energy-level diagram for $\vec{E} \parallel \langle 100 \rangle$ in Fig. 17 using the above parameters. To separate the various symmetries, we show all E levels as solid lines, all A_1 levels as dashed lines, all B_1 levels as dot-dash lines, and all B_2 levels as dotted lines. The allowed PER transitions for $E_{rf} \parallel E_{dc}$ are between states of the same symmetry.

At zero electric field, with η dominant as above, the energy levels are ordered T_{2u}, E_g, T_{2g}, T_{1u}, and A_{1g} in each multiplet. With increasing electric field the levels in each multiplet split as expected for a $\langle 110 \rangle$ system, but at relatively low fields of 20–30 kV/cm, energy levels from the two multiplets begin to cross. The important "crossings" to note are those of states with the same symmetry. In general, there is some interaction between such states and a repulsion of energy levels occurs. A good example is observed at 33 kV/cm for the $2A_1$ and $3A_1$ states. The minimum separation of these levels gives rise to a turn around point at a frequency of 16 GHz. In some cases the coupling between such states is so small that the splitting of the levels is not visible on the scale of this figure. Two examples occur in the 20–30 kV/cm range; for the $3E$ and $4E$ states and for the $2B_1$ and $3B_1$ states.

A comparison of the computer predictions with the data, using the above parameters, is given in Figs. 18–20. Because of the large number of lines in the spectrum these figures are unfortun-

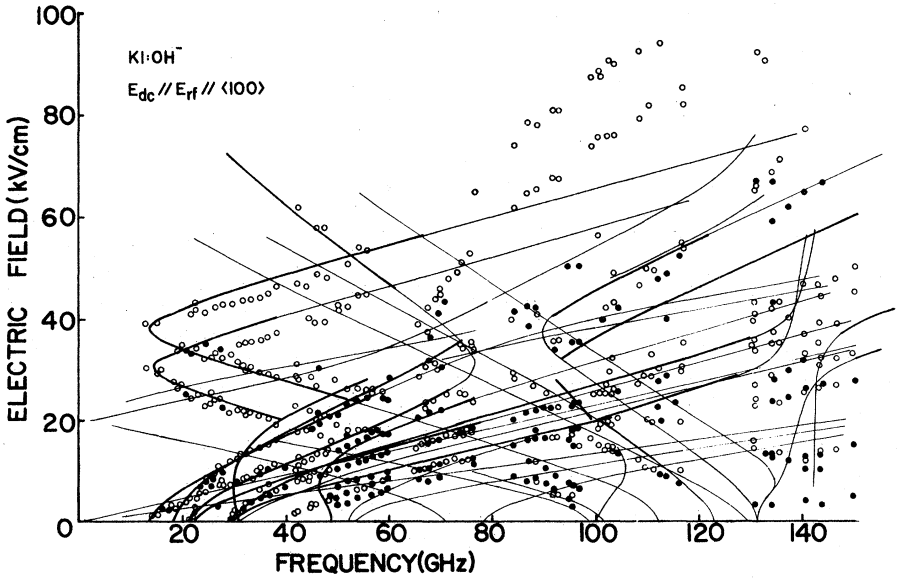

FIG. 18. Comparison of the experimental data with $\langle 110 \rangle$-$\langle 1\bar{1}0 \rangle$ tunneling model for $E_{dc} \parallel E_{rf} \parallel \langle 100 \rangle$ using the following parameters: $\epsilon = 140$ GHz, $p = 1.25\ e$Å, $p' = 2.15\ e$Å. $\eta, \mu, \nu, \sigma = 8.25, 1, 0, 0$ GHz, respectively; $\eta', \mu', \nu', \sigma' = 13.5, 2.4, 0, 0$ GHz, respectively; η'', μ'', ν'', $\sigma'' = 5, 0, 0, 0$ GHz, respectively. The strongest theoretical line intensities are indicated by the heavy lines.

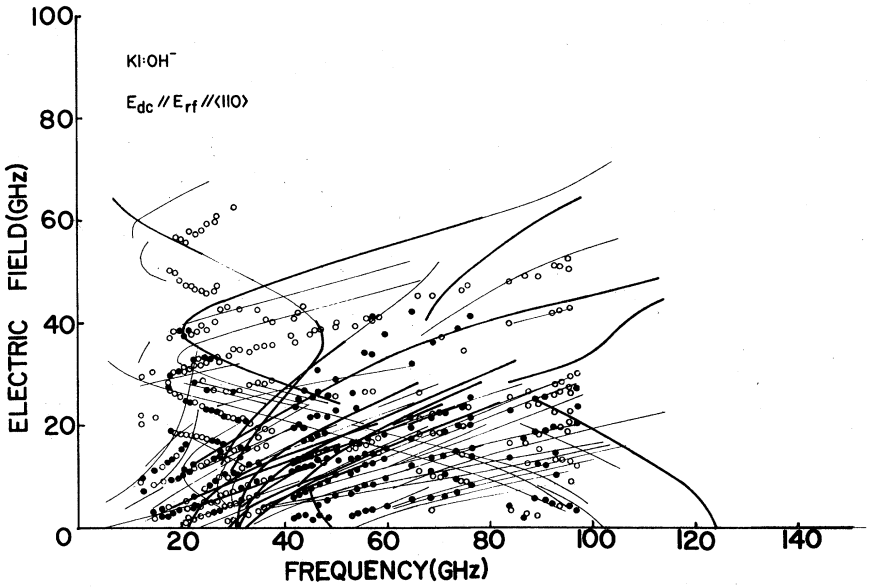

FIG. 19. Experimental data compared with the two-multiplet model for $\vec{E}_{dc} \| \vec{E}_{rf} \| \langle 110 \rangle$ using the same parameters as in Fig. 18.

ately quite complicated and it is helpful to refer to Figs. 7–9 to follow the various experimental lines.

The overall features of the calculations agree quite well with the data; the backward lines, the approximate positions of most of the zero-field splittings, and the presence of lines that become field independent at high frequencies. The following points give the other major results from this analysis: (i) η and η' are the dominant tunneling parameters; allowing any other parameters (or pairs of parameters) to dominate give spectra in serious disagreement with the data. (ii) Part of the uncertainty in ϵ and the tunneling parameters is due to the fact that the ZFS within each multiplet also depend on ϵ. (iii) Some of the weaker ZFS are poorly fit. The addition of small amounts of other parameters might correct this, but a clear determination would require better data and further analysis with this model is therefore not justified at present. (iv) The intramultiplet parameters are determined least accurately. Although the positions of the backward lines are reasonably explained assuming only $\eta'' \neq 0$, the intensities of some lines are not correct. This is likely a reflection of the neglect of μ'', ν'', and σ''. (v) The greatest inconsistency between this model and the data is the observation of two strong lines (9 and 10 of Fig. 7) that have no counterpart in the predicted allowed lines. One might first suspect

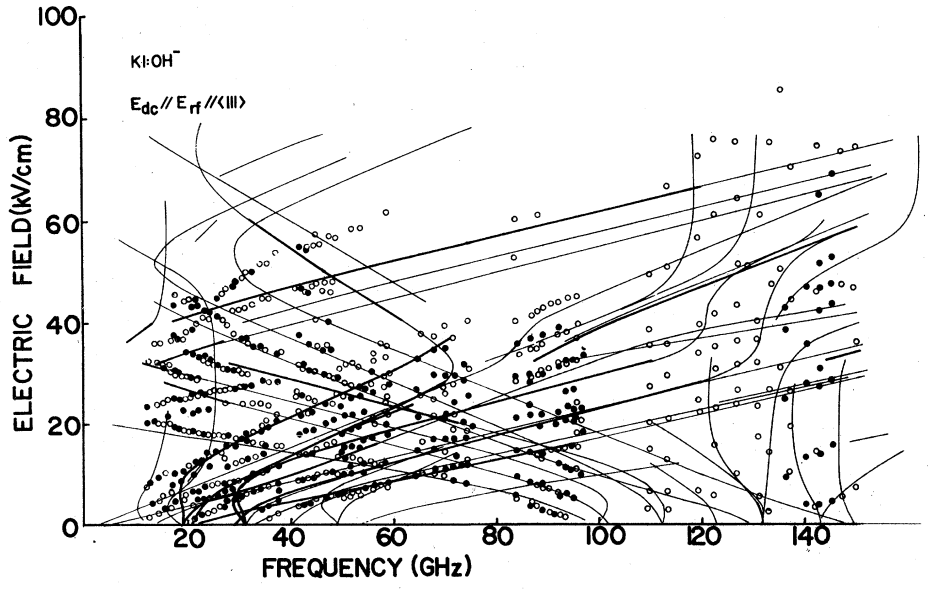

FIG. 20. Experimental data compared with the two-multiplet model for $\vec{E}_{dc} \| \vec{E}_{rf} \| \langle 111 \rangle$ using the same parameters as in Fig. 18.

that these lines arise from some other impurity. However, since they were observed with the same relative intensities in samples from four different boules, it is highly unlikely that they are not part of the OH^- spectrum. One might also consider the possibility that they are strain-allowed lines, since it has been shown that internal strain can make forbidden transitions acquire appreciable intensity. A check of the forbidden transitions for the ⟨110⟩-⟨110⟩ model does indeed show lines with the distinctive electric field dependence of lines 9 and 10 although shifted somewhat in frequency. Whether or not some distribuiton of internal strains could also explain the high intensities of these lines would require considerable work and has not been determined. To make forbidden transitions become comparable in intensity to the dominant lines of the spectra via internal strains does not seem likely.

VI. DISCUSSION AND POSSIBLE ORIGIN OF UPPER STATES

The above analysis shows that most of the data can be understood in terms of two ⟨110⟩-dipole multiplets with dipole moments $p = 1.25$ Å and $p' = 2.15$ Å in the lower and upper multiplet, respectively. The existence of an additional multiplet is clearly established by the high-frequency splittings and the backward lines and occurs approximately 140 GHz above the lower multiplet. The slopes of the lines for the three orientations of electric field are internally very consistent for ⟨110⟩-directed dipoles with the above values of p and p'. However, the two lines in the ⟨100⟩ data which do not appear to fit into this scheme very well suggest that this is not the complete story and extensions or changes are likely necessary to understand the $KI:OH^-$ system fully. These lines, which occur a little too high in frequency for the lower multiplet and are too low in frequency to be intramultiplet transitions, may in fact be evidence for additional energy levels or another multiplet only 60–70 GHz above the ground multiplet.

Before considering how the model should be extended or changed it is useful, now that the general features of the upper states are known, to consider their origin. There are numerous ways in which several multiplets might occur, we first list them and then discuss them as they pertain to the $KI:OH^-$ system.

1. Librational modes

These are torsional oscillations in each of the directed potential wells. The dipole can librate about its equilibrium orientation in two different ways which may or may not be degenerate. This requires two additional states per dipole well.

2. Center-of-mass vibrational modes

These represent an oscillation of the c.m. of the OH^- ion and might occur in two different ways. If the off-center potential wells for the OH^- ion are deep, a radial center-of-mass (c.m.) oscillation may occur in each well. On the other hand is the potential at the center of the I^- cavity is low enough that the excited states occur above the barrier, then the c.m. oscillation might be across the entire I^- cavity.

3. Combinations of an off-center dipole with the molecular OH^- dipole

Here there are many different possibilities depending on how the dipoles couple together. Since we do not know how these dipoles couple quantum mechanically, we consider only general cases.

(a) The two dipoles essentially couple in parallel or antiparallel, with one of these combinations occurring at a higher energy. This clearly would give two multiplets with two dipole moments but depending on the coupling scheme, the measured moments may not be the exact sum and difference of the off-center and molecular dipole moments.

(b) The two dipoles couple at some well-defined angle that is the same for all off-center orientations. Two types of tunneling can occur, a rotation of the molecular dipole about an off-center axis or a rotation of the off-center position. If one of these tunneling processes is much faster than the other, the energy levels will be grouped into multiplets, but these multiplets will be different from the usual models considered for paraelectric systems. The effective-dipole moment can also have a different orientation than either the off-center or molecular dipole, e.g., if the off-center and molecular dipoles couple at an angle of 90° and orient along the ⟨100⟩ axes, then when these dipoles are approximately equal in magnitude, the effective dipole is approximately along a ⟨110⟩ crystal direction.

(i) Off-center dipole along ⟨100⟩. Here there are four equivalent orientations of the molecular dipole about the off-center axis and one therefore requires 24 states. If the tunneling rotation of the molecular dipole is much faster than the tunneling of the off-center position, then at zero field three multiplets will occur. The separation of the multiplets will depend on the molecular-dipole tunneling parameters and the splittings within a multiplet will depend on the off-center tunneling parameters.

(ii) Off center along ⟨111⟩. Here there are three equivalent positions for the molecular dipole and hence again 24 states are required. When the molecular dipole tunneling is much larger than the off-center position tunneling, two multiplets will occur.

(iii) Off-center along ⟨110⟩. Here there are only two equivalent positions of the molecular dipole, but again a total of 24 states. Two multiplets will form if the molecular dipole tunneling is much larger than the off-center position tunneling.

(c) A combination of (a) and (b) above, or the possibility that the angle between the two dipoles can have several values, would of course lead to additional multiplets.

For the first two models above, one can make estimates of the librational- and vibrational-mode splittings and hence test whether or not such models are consistent with the observed splittings of 140 GHz. From such considerations, the torsional-oscillator model clearly does not appear viable. A lower estimate for the librational modes is $\nu > 500$ GHz—far too large to explain the observed results. This is of course, the same difficulty that was encountered earlier in connection with the hindered-rotor model. Unless there is a huge mass enhancement by the phonon dressing of the dipole, which we feel is unlikely, this model can be ruled out.

For the vibrational c.m. motion, in a deep-side potential well, a similar result is obtained. Using a square well of dimension 1 Å, the vibrational frequency is about 880 GHz, again too high to explain the observed splitting, and this model is therefore also eliminated. The c.m. vibration across the entire I^- cavity is not so easily eliminated but, now that the intermultiplet splitting is established, this model is no longer very promising. As pointed out earlier,[3] the first excited state in a square well of dimension 2 Å is about 220 GHz—clearly the correct order of magnitude but a little too high to explain the observations. An estimate using a double square well with a low central barrier gave a still higher frequency for the vibrational state. Since the assumption of a 2-Å width is probably already an overestimate, it appears unlikely that the vibrational-mode frequency can be reduced to 140 GHz for this system. Yet another argument against this model is the magnitude of the dipole moment for the upper states. If the vibrational mode is across the entire I^- cavity then the dipole moment should arise from the intrinsic molecular moment and a moment of about 0.9 e Å (i.e., comparable to the dipole moment observed in most other alkali halides) would be expected. The much larger experimental value, $p' \cong 2.15$ e Å would be difficult to explain within this model. Thus, on the basis of such arguments we also eliminate the c.m. vibration model from further consideration.

On the other hand, the coupled-dipole models appear quite promising, since, if OH^- goes off center in KI two dipole moments, the off-center moment and the intrinsic molecular moment, must be present. In the case of parallel and antiparallel coupling, two multiplets with the same dipole orientation would result, and should be well described by the two-multiplet model we have used. If we interpret our data in terms of such a model then the larger dipole moment (upper multiplet) represents the two dipoles in parallel and the smaller dipole moment, the dipoles antiparallel to each other. However, we cannot separate the components since we do not know whether the off-center position, and hence the off-center dipole moment, is the same in each case.

The other coupled-dipole models are slightly more complicated and have several additional features—there may be more than two multiplets—each multiplet will not have the form—the level splittings of a given multiplet in the presence of an electric field may depend on both dipole moments, and new types of tunneling parameters will be necessary. We point out that the observed slopes can be accounted for using ⟨100⟩ -oriented off-center impurities whose molecular-dipole moments are oriented at 90° to the off-center directions.

The coupled-dipole models can explain in a very natural way the presence of additional multiplets of energy levels and of two distinct dipole moments. This, together with the difficulty of explaining the small intermultiplet splitting using the librational or vibrational models leads us to interpret our data as *evidence for a coupled-dipole model*. To our knowledge this is the first paraelectric system to exhibit such behavior. Whether the models in which the dipoles couple at some angle can provide a better explanation of the data than the two-multiplet parallel-antiparallel model requires considerable additional analysis. Before proceeding with further calculations, however, it is useful to have some additonal information about this system. Phonon spectroscopy measurements of the KI:OH^- system are now underway,[26] and further analysis of the PER data will therefore be postponed until the phonon experiments are completed.

VII. SUMMARY AND CONCLUSIONS

The interesting features of the low-frequency microwave absorption for the KI:OH paraelectric center prompted a thorough experimental investigation of this system over the 12–150 GHz range. Our new data confirm the existence of an additional multiplet about 140 GHz above the ground state and show that two different dipole moments are associated with this center.

We analyzed our data in terms of a two-multiplet model and found that only two ⟨110⟩ multiplets,

with dipole moments 1.25 and 2.15 e Å in the lower and upper multiplets, respectively, can explain our results. The general agreement between data and this model is quite good—the positions of the backward lines, the slopes of the lines and the positions of the main ZFS can be explained for all but two lines in the $\vec{E}\|\langle 100\rangle$ data. The dominant tunneling parameters for this model are the nearest-neighbor (60° rotation) parameters—both for the individual multiplets and for the intermultiplet matrix elements.

We have considered a number of models which might yield such features and concluded that the only viable models are those in which the coupling of the off-center dipole moment and the molecular-dipole moment is considered. In terms of such models, the two-multiplet model represents the dipoles coupled parallel or antiparallel to one another along a $\langle 110\rangle$ crystal direction. The states with the dipoles coupled in parallel would form the upper multiplet. However, the difficulty in explaining the two additional strong lines in the $\vec{E}\|\langle 100\rangle$ data points out that the model is not complete and that the models in which the dipoles couple at an angle must be considered. Further analysis, however, will wait until phonon experiments, now underway, are completed.

At low electric fields we have examined the line shape of the swept-frequency data. The symmetry of the absorption line at low electric fields (where we had expected nonsymmetric lines) clearly indicates that a distribution of internal electric fields is not the primary broadening mechanism. Further, from simple calculations for a four-fold multiplet it appears unlikely that the stress interaction alone can account for the symmetric shape either and further investigations of the broadening mechanisms are needed.

ACKNOWLEDGMENTS

We wish to thank Professor F. Lüty, Professor G. Dick, and Professor H. Shore for helpful discussions and suggestions in the course of these experiments, and R. Russell for his assistance in the laboratory. This work was supported by the NSF under Grant No. 443150-21249.

APPENDIX A: MATRIX ELEMENTS FOR THE $\langle 110\rangle$ SYSTEMS

The symmetric matrix for the crystal-field Hamiltonian $\mathcal{H}_c$ in terms of the tunneling elements defined in Eq. (4.2), is

$$\mathcal{H}_c(\eta,\mu,\nu,\sigma)=\begin{pmatrix}
0 & \sigma & \mu & \mu & \nu & \eta & \eta & \nu & \nu & \eta & \eta & \nu \\
 & 0 & \mu & \mu & \eta & \nu & \nu & \eta & \eta & \nu & \nu & \eta \\
 & & 0 & \sigma & \nu & \eta & \eta & \nu & \eta & \nu & \nu & \eta \\
 & & & 0 & \eta & \nu & \nu & \eta & \nu & \eta & \eta & \nu \\
 & & & & 0 & \sigma & \mu & \mu & \eta & \nu & \eta & \nu \\
 & & & & & 0 & \mu & \mu & \nu & \eta & \nu & \eta \\
 & & & & & & 0 & \sigma & \eta & \nu & \eta & \nu \\
 & & & & & & & 0 & \nu & \eta & \nu & \eta \\
 & & & & & & & & 0 & \sigma & \mu & \mu \\
 & & & & & & & & & 0 & \mu & \mu \\
 & & & & & & & & & & 0 & \sigma \\
 & & & & & & & & & & & 0
\end{pmatrix}. \quad \text{(A1)}$$

The diagonal elements in the presence of an electric field $\vec{E}=(E_x,E_y,E_z)$ are given by

TABLE II.

$\langle 100\rangle$ Dipoles	$\langle 110\rangle$ Dipoles	$\langle 111\rangle$ Dipoles
$E\|\|\langle 100\rangle$		
A:slope $h/2p$ via μ	A:slope $h/\sqrt{2}p$ via μ,ν,σ	A:slope $\sqrt{3}h/2p$ via η,μ,ν
B:slope h/p via η	B:slope $\sqrt{2}h/p$ via η,ν	
$E\|\|\langle 110\rangle$		
A:slope $h/\sqrt{2}p$ via η,μ	A:slope $h/\sqrt{2}p$ via σ	A:slope $\sqrt{6}h/4p$ via μ,ν
B:slope $\sqrt{2}h/p$ via η	B:slope $2h/3p$ via ν	B:slope $\sqrt{6}h/2p$ via η,μ
	C:slope h/p via η,μ,ν,σ	
	D:slope $2h/p$ via η,ν	
$E\|\|\langle 111\rangle$		
A:slope $\sqrt{3}h/2p$ via η,μ	A:slope $\sqrt{6}h/4p$ via ν,σ	A:slope $h/2p$ via ν
	B:slope $\sqrt{6}h/2p$ via η,μ,ν	B:slope $3h/2p$ via η,ν
		C:slope $3h/4p$ via μ

$$
\begin{aligned}
&\langle 1|\,\mathcal{H}_{dc}|1\rangle = -p(E_x+E_y)/\sqrt{2}\,,\\
&\langle 2|\,\mathcal{H}_{dc}|2\rangle = p(E_x+E_y)/\sqrt{2},\\
&\langle 3|\,\mathcal{H}_{dc}|3\rangle = -p(E_x-E_y)/\sqrt{2}\,,\\
&\langle 4|\mathcal{H}_{dc}|4\rangle = p(E_x-E_y)/\sqrt{2}\,,\\
&\langle 5|\,\mathcal{H}_{dc}|5\rangle = p(E_x+E_z)/\sqrt{2}\,,\\
&\langle 6|\,\mathcal{H}_{dc}|6\rangle = -p(E_x+E_z)/\sqrt{2}\,,\\
&\langle 7|\,\mathcal{H}_{dc}|7\rangle = -p(E_x-E_z)/\sqrt{2}\,,\\
&\langle 8|\,\mathcal{H}_{dc}|8\rangle = p(E_x-E_z)/\sqrt{2}\,,\\
&\langle 9|\mathcal{H}_{dc}|9\rangle = p(E_y+E_z)/\sqrt{2}\,,\\
&\langle 10|\,\mathcal{H}_{dc}|10\rangle = -p(E_y+E_z)/\sqrt{2}\,,\\
&\langle 11|\mathcal{H}_{dc}|11\rangle = -p(E_y-E_z)/\sqrt{2}\,,\\
&\langle 12|\,\mathcal{H}_{dc}|12\rangle = p(E_y-E_z)/\sqrt{2}\,.
\end{aligned}
\tag{A2}
$$

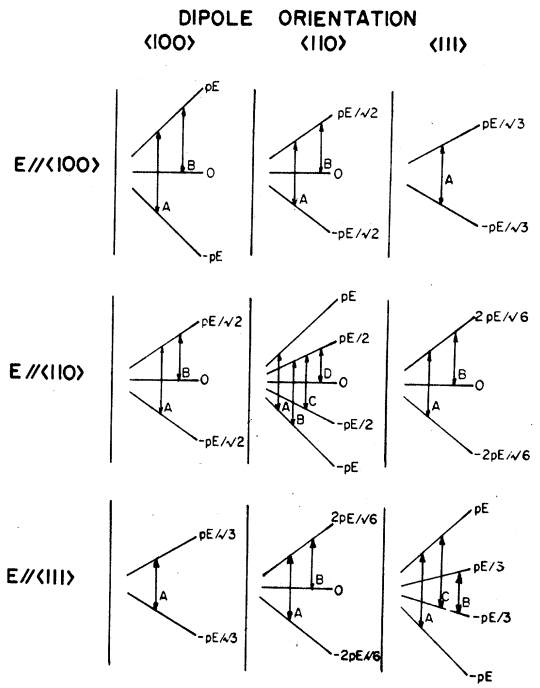

FIG. 21. Expected high-field energy-level behavior for the three single-multiplet tunneling models. The splittings of each energy level, caused by tunneling, are ignored.

APPENDIX B

A summary of expected slopes (of resonant electric field plotted against frequency) is given in Table II for the single-multiplet tunneling models. The resonance notation is illustrated in Fig. 21. The tunneling parameters which make each transition nonzero in first order are indicated.

APPENDIX C

Figure 22 shows the approximate energy levels which one expects the ⟨110⟩-⟨110⟩ two-multiplet model to have in the large electric-field approximation, ignoring the tunneling splitting which is normally present in each level. For convenience all the energy levels are drawn crossing, even though transitions are indicated between them. The various types of energetically distinct *backward* lines are indicated and it should be noted that not all the indicated lines will be backward, for example, in the $\vec{E}\|\langle 100\rangle$ diagram either D or E will

TABLE III. Backward line slopes for a ⟨110⟩-⟨110⟩ model. The tunneling parameters making each transition allowed to first order are indicated ("directly" indicates a transition from the ground to excited state in the same off-center orientation).

E||⟨100⟩	
A:slope $-\sqrt{2}h/p'$	via η'',ν''
B:slope $-\sqrt{2}h/(p'+p)$	via μ'',ν'',σ''
C:slope $-\sqrt{2}h/p$	via η'',ν''
D:slope $-\sqrt{2}h/(p'-p)$	via η'',μ'', and directly
E:slope $-\sqrt{2}h/(p-p')$	via η'',μ'', and directly
E||⟨110⟩	
A:slope $-2h/(p-2p')$	via η''
B:slope $-h/p'$	via μ''
C:slope $-2h/p'$	via η'',ν''
D:slope $-2h/(2p'+p)$	via ν''
E:slope $-2h/(p+p')$	via η'',μ'',ν'',σ''
F:slope $-2h/p$	via η'',ν''
G:slope $-h/(p'+p)$	via σ''
H:slope $-h/p$	via μ''
J:slope $-2h/2p-p')$	via η''
K:slope $-2h/(p'+2p)$	via ν''
L:slope $-h/(p'-p)$	directly
M:slope $-2h/(p-p')$	via η'',μ'',ν'', and directly
N:slope $-h/(p-p')$	directly
P:slope $-2h/(p'-p)$	via η'',μ'',ν'', and directly
E||⟨111⟩	
A:slope $-\sqrt{6}h/2p'$	via η'',μ'',ν''
B:slope $-\sqrt{6}h/2(p+p')$	via ν'',σ''
C:slope $-\sqrt{6}h/2p$	via η'',μ'',ν''
D:slope $-\sqrt{6}h/2(p'-p)$	via η'' or directly
E:slope $-\sqrt{6}h/2(p-p')$	via η'' or directly

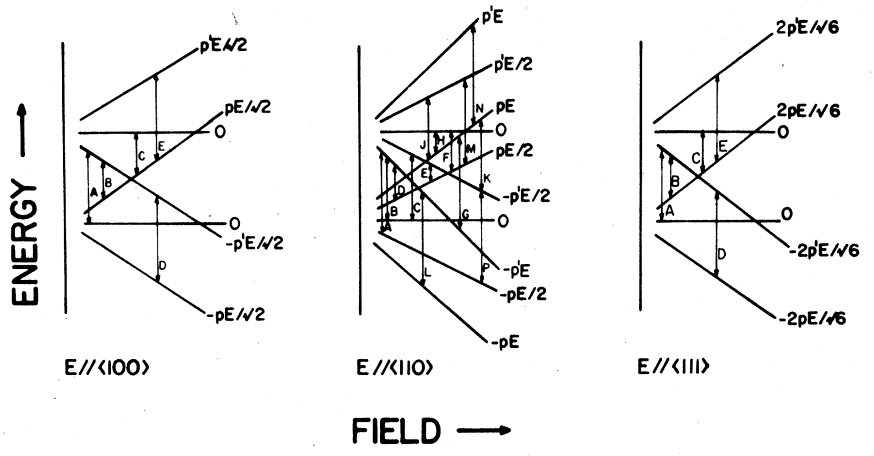

FIG. 22. Energy levels for the ⟨110⟩-⟨110⟩ two-multiplet model in the high-electric-field approximation. Splittings at crossings of energy levels have been omitted. The various types of backward lines are indicated.

be backward, but not both, depending upon whether p or p' is the greater. In addition it has been assumed that p and p' are of the same order of magnitude, if $p \gg p'$ or vice versa there will exist backward lines for $\vec{E} \| \langle 110 \rangle$ other than those listed. Table III lists the high-field slope of each transition indicated in Fig. 15, and the matrix elements making these transitions allowed to first order.

*Present address: Millimeter Diode Lab, Dept. of Electrical Engineering, University College, Cork, Ireland.

[1]B. Wedding and M. Klein, Phys. Rev. 177, 3, 1274 (1969).
[2]S. Kapphan and F. Lüty J. Phys. Chem. Solids 34, 969 (1973).
[3]F. Bridges, Solid State Commun. 13, 1877 (1973).
[4]R. Hundhausen, R. Osswald, and H. C. Wolf, Phys. Status Solidi B 63, 197 (1974).
[5]F. Bridges, Phys. Status Solidi B 65, 743 (1974).
[6]W. M. Kelly and F. Bridges, Solid State Commun. 20, 119 (1976).
[7]M. Gomez, S. P. Bowen, and J. A. Krumhansl, Phys. Rev. 153, 1009 (1967).
[8]F. Bridges, Rev. Sci. Instrum. 45, (1974).
[9]W. Gordy and W. C. King, Phys. Rev. 93, 407 (1954).
[10]The spectrum was also checked with the sample relatively loosely held. It was noisy but exhibited no line shifts indicating that the applied stress was negligible here.
[11]T. G. Phillips and K. B. Jefferts, Rev. Sci. Instrum. 44, 1009 (1973).
[12]S. B. Cohn, Proc. I. R. E. 35, 783 (1947).
[13]F. Bridges, Phys. Rev. B 5, 3321 (1972).
[14]For a review of paraelectricity, see F. Bridges, Crit. Rev. Solid State 5, 1 (1975); V. Narayanamurti and R. O. Pohl, Rev. Mod. Phys. 42, 201 (1970).
[15]L. Pauling, Phys. Rev. 36, 430 (1930).
[16]A. F. Devonshire, Proc. R. Soc. Lond. A 153, 601 (1936).
[17]H. U. Beyeler, Phys. Status Solidi B 52, 419 (1972).
[18]H. B. Shore, Phys. Rev. 151, 570 (1966).
[19]P. Sauer, O. Shirmer, and J. Schneider, Phys. Status Solidi 16, 79 (1966).
[20]B. Dischler, Z. Naturforsch. A 25, 1844 (1970); 28, 938 (1973).
[21]H. B. Shore and L. M. Sander, Phys. Rev. B 3, 1472 (1971); 6, 1551 (1972).
[22]R. Pirc and P. Gosar, Phys. Kondens. Mater. 9, 377 (1969).
[23]R. Timme, B. Dischler, and T. Estle, Phys. Rev. B 1, 1610 (1970).
[24]R. A. Herendeen and R. H. Silsbee, Phys. Rev. 188, 645 (1969).
[25]M. Deigen, M. Glinchuk, and V. Vikhnin, Sov. Phys. Solid State 13, 2270 (1972).
[26]W. Zoller and F. Bridges, Bull. Am. Phys. Soc. 23, 437 (1978); and unpublished.